Results in Physics 61 (2024) 107755

Contents lists available at ScienceDirect

Results in Physics

journal homepage: www.elsevier.com/locate/rinp

Exploring optical tomography dynamics for a dissipative coherent cavity in interaction with two-level atomic system

A.-B.A. Mohamed [a], T.A. Alrebdi [b], F. Alkallas [b], A.-H. Abdel-Aty [c,*], H. Eleuch [d,e,f]

[a] Department of Mathematics, College of Science and Humanities, Prince Sattam bin Abdulaziz University, Alkharj, Saudi Arabia
[b] Department of Physics, College of Science, Princess Nourah bint Abdulrahman University, P.O. Box 84428, Riyadh 11671, Saudi Arabia
[c] Department of Physics, College of Sciences, University of Bisha, PO Box 344, Bisha 61922, Saudi Arabia
[d] Department of Applied Physics and Astronomy, University of Sharjah, Sharjah, 27272, United Arab Emirates
[e] College of Arts and Sciences, Abu Dhabi University, Abu Dhabi 59911, United Arab Emirates
[f] Institute for Quantum Science and Engineering, Texas A&M University, College Station, TX 77843, USA

ARTICLE INFO

Keywords:
Cavity damping
Optical tomography
Master equation
Coherence dynamics

ABSTRACT

In this paper, we explore the optical tomography and quantum coherence dynamics for a coherent cavity field interacting with a two-level atom via intensity dependent coupling. We derive a specific solution to the master equation for the Jaynes–Cummings model, considering cavity damping. This solution reveals how the atom coherent-cavity interactions can produce new coherent states when the initial dissipative cavity-field state is coherent state or even coherent state. The effects of the atom-coherent-cavity interactions and the cavity damping, on the dynamics of the initial coherent state optical tomography and coherence is examined. In addition to the nonclassical properties, the atom-cavity interactions have a remarkable capacity to form distinct cavity field states linked to certain optical tomography distributions. Additionally, we investigate the maximal optical tomography dynamics for coherent state and even coherent state considering a range of cavity damping and detuning values.

Introduction

The optical tomography is a powerful tool for estimating the quantum state properties. It is directly dependent on the quantum state density matrix. To encode quantum information, several approaches for reconstructing optical tomography based on Wigner quasiprobability distribution [1] (which in turn is related monotonically to the coherent field state density operator and their probability distributions [2]) and homodyne detection of optical quadratures (which also is related monotonically to the homodyne detector) [3–6] are introduced. Quantum tomography of a homodyne detector and a pulsed homodyne detection with poor detection efficiency has been achieved experimentally [7,8].

Based on a appropriate measurement set, the quantum state tomography (QST) can determine an unknown quantum state [9] and extracts all possible quantum state information contained in the density operator. QST is of great importance for quantum information [10]. The optical tomography has been used to protect several quantum phenomena [11–13] as: phase space non-classicality, nonclassical correlations, and coherence. Optical tomography has been investigated over a wide range of quantum states resulting from many real systems. The optical homodyne tomography of time-evolved states inside a single-mode field including a Kerr medium was specifically examined for coherent states, m-photon-added coherent states, and even and odd coherent states [14]. Optical tomography has been expanded to investigate excited coherent states associated with deformed oscillators using the homodyne deformed quadrature operators [15]. In addition, neural-network quantum state tomography has been successfully implemented in a two-qubit experiment [16]. Furthermore, optical tomography research includes the examination of time-dependent dissipative coherent states that occur due to the evolution of dissipative coherent fields interacting with a qubit, including even and odd-coherent fields [17].

Producing coherent cavity field states through interactions with a two-level atomic system can be realized by using various quantum physical models, such as the Jaynes–Cummings (JC) model [18] and the Tavis–Cummings model [19]. JC-Model is extended to describe dissipative atom-cavity interactions in open quantum systems [20, 21] such as trapped ions [22–24] and superconducting-quantum circuits [25–27]. The quantum states created by atom–atom and atom-cavity interactions have been employed to realize various quantum phenomena [28–30]. Tavassoly and his group constructed the JCM and TCM for various physical systems, taking into account the influence

* Corresponding author.
E-mail address: amabdelaty@ub.edu.sa (A.-H. Abdel-Aty).

https://doi.org/10.1016/j.rinp.2024.107755
Received 6 September 2023; Received in revised form 26 April 2024; Accepted 9 May 2024
Available online 11 May 2024

of coherence and the environment on the quantum properties of the proposed models [31–34].

In open system, dissipation and decoherence emerge due to the irreversible coupling of the system to the surrounding environment that eventually affect nonclassical effects such as quantum correlations and coherence. Therefore, the effects of dissipation and decoherence have been investigated in open quantum systems [35–41]. The investigations of the dissipation and decoherence effects on the optical homodyne tomography of generated states due to zero-temperature master equation are limited. Previous studies have analyzed decoherence effects on optical homodyne tomography for a phase damping model with initial coherent states [14,17]. Furthermore, the dynamics of optical homodyne tomography have been analyzed by exploring intrinsic decoherence effects involving two-photon interactions with qubit-resonator interactions [42].

The motivations behind this work are: Firstly, the precise dynamics of open atom-field systems remain an unsolved problem with crucial consequences for identifying the stable state of different quantum phenomena. Notably, optical tomography and quantum coherence research into non-classicality are critical in the context of dissipative qubit-cavity interactions. Despite their importance, there are a relatively limited number of studies that address optical tomography of coherent field states without accounting for dissipation effects. Secondly, existing quantum tomography experimental investigations, such as homodyne detectors and pulsed homodyne detection, are constrained by poor detection efficiency. We present an analytical description of the interaction of a dissipative cavity field and a two-level atom under off-resonant conditions with intensity-dependent coupling in this study. Our goal is to explore the non-classicality'optical tomography and quantum coherence of the coherent field states that are produced by this interaction utilizing the optical tomography. Therefore, we examine the nonclassical features of optical tomography using a homodyne detector (attributed to intensity-dependent atom-field interactions). This investigation is dependent on the von-Neumann entropy coherence of the cavity field at distinct time points, which correspond to partial and maximum photon-field mixedness.

The physical model and its solution is presented in Section "Physical model and its solution". In Section "Optical tomography" the definition of the optical tomography is introduced. While the optical tomography distributions of the generated coherent field states are introduced in Section "Optical tomography dynamics". Finally, our conclusion is addressed in Section "Conclusions".

Physical model and its solution

In order to investigate the optical tomography dynamics of the generated dissipative coherent cavity field due to its interaction with a two-level atomic system, we use the following master equation,

$$\frac{d\hat{\rho}(t)}{dt} = -i[\hat{H},\hat{\rho}(t)] + \gamma([a\hat{\rho}(t),\hat{a}^\dagger] + [\hat{a},\hat{\rho}(t)\hat{a}^\dagger]), \tag{1}$$

where γ is the dissipative cavity field damping rate. Here, we consider a cavity field (that filled by coherent field/ two-superposed-opposite-coherent fields $|\pm\alpha\rangle$) interacting with a two-level atom, nonlinearly, via intensity-dependent coupling [43]. Therefore, the atom-cavity Hamiltonian is given by: $\hat{H} = \frac{\omega_\circ}{2}[|1\rangle\langle 1| - |0\rangle\langle 0|] + \omega\hat{a}^\dagger\hat{a} + \lambda[\hat{a}\sqrt{\hat{a}^\dagger\hat{a}}|1\rangle\langle 0| + \sqrt{\hat{a}^\dagger\hat{a}}\,\hat{a}^\dagger|0\rangle\langle 1|]$, where ω represents the frequency of the cavity field having the annihilation $\hat{a}$ and the creation $\hat{a}^\dagger$ operators. $\omega_\circ$ designs the atomic frequency between its excited $|1\rangle$ and ground $|0\rangle$ states. The atom-cavity detuning is identified by $D = (\omega_\circ - \omega)/2$. λ is the atom-field interaction coupling. The intensity-dependent coupling can be realized by different superconducting circuits [44–46] as well as trapped-ion interactions [22]. The intensity dependent nanomechanical resonator is described by the annihilation operator $\hat{a}\sqrt{\hat{a}^\dagger\hat{a}}$ [44] and by the annihilation operator of the deformed field mode's nanomechanical resonator $\hat{a}f(\hat{a}^\dagger\hat{a})$. [45]. While in [46], the nonlinearity in atom-field coupling has been realized by the k-photon-mediated coupling between the charge qubit and the microwave field.

Here, using the dressed state representation (DSR) technique, an analytical expression of Eq. (1) can be derived. considering the high$-Q$ cavity ($\gamma \ll \lambda$) regime [36]. In atom-field state subspace spanned by $|\varpi_1\rangle = |1,n\rangle(n = 0,1,2,\ldots)$ and $|\varpi_2\rangle = |0,n+1\rangle$, the atom-cavity Hamiltonian dressed states are:

$$|S_n^\pm\rangle = X_n^\pm|\varpi_1\rangle \pm X_n^\mp|\varpi_2\rangle,\, X_n^\pm = \frac{1}{\sqrt{2}}\sqrt{1 \pm \frac{D}{\eta_n}},\, \eta_n = \sqrt{D^2 + \lambda^2(n+1)^2} \tag{2}$$

According to the eigenvalue equations, $H|S_n^\pm\rangle = E_n^\pm|S_n^\pm\rangle$ and $H|0,0\rangle = -\frac{\omega_\circ}{2}|0,0\rangle$, the eigenvalues of the atom-cavity Hamiltonian are given by: $E_n^\pm = \mu_n \pm \eta_n, \mu_n = \omega(n+\frac{1}{2})$ In the DSR method, the cavity field operators, $\hat{a}$ and $\hat{a}^\dagger\hat{a}$ operators,need to be expressed in function of the dressed state operators. We use then the canonical representation: $R(t) = e^{i\hat{H}t}\hat{\rho}(t)e^{-i\hat{H}t}$ and neglecting the oscillatory terms [36]. Therefore, Eq. (1) for $R(t)$ is given by:

$$\begin{aligned}\dot{R}(t) &= 2\gamma\sum_{n=1}\{W_n^{+2}\hat{Y}^{++} + W_n^{-2}\hat{Y}^{--} + G_n^{+2}\hat{Y}^{+-} + G_n^{-2}\hat{Y}^{-+}\}\\ &\quad -\gamma\sum_{n=0}\{[\hat{Z}^+ + \hat{Z}^-]R(t) + R(t)[\hat{Z}^+ + \hat{Z}^-]\},\end{aligned} \tag{3}$$

with $Y^{\pm\pm} = |S_{n-1}^\pm\rangle\langle S_n^\pm|R(t)|S_n^\pm\rangle\langle S_{n-1}^\pm|$, $\hat{Z}^\pm = V_n^\mp|S_n^\pm\rangle\langle S_n^\pm|$, $V_n^\mp = [n + (X_n^\mp)^2]$, and

$$W_n^\pm = \sqrt{n}\,X_{n-1}^\pm X_n^\pm + \sqrt{n+1}X_{n-1}^\mp X_n^\mp, \tag{4}$$

$$G_n^\pm = \sqrt{n}\,X_{n-1}^\pm X_n^\mp - \sqrt{n+1}X_{n-1}^\mp X_n^\pm. \tag{5}$$

The off-diagonal elements $R_{mn}^{\pm\pm}(t) = \langle S_m^\pm|R(t)|S_n^\pm\rangle$ of the matrix $R(t)$ are:

$$R_{mn}^{\pm\pm}(t) = \exp[-\gamma(m+n+\Phi_m^{\mp2}+\Phi_n^{\mp2})]R_{mn}^{\pm\pm}(0), \quad \forall\ m \neq n. \tag{6}$$

But, the diagonal elements of the atom-cavity matrix $R(t)$, $R_n^\pm(t) = \langle S_n^\pm|R(t)|S_n^\pm\rangle$, are verifying:

$$\dot{R}_n^\pm(t) = 2\gamma H_{n+1}^{\pm2}R_{n+1}^\pm(t) + 2\gamma G_{n+1}^{\pm2}R_{n+1}^\mp(t) - 2\gamma V_n^\mp R_n^\pm(t), \tag{7}$$

with a solution in the form

$$R_n^\pm(t) = e^{-2\gamma V_n^\mp t}R_n^\pm(0) + 2\gamma\int_0^t e^{2\gamma V_n^\mp\tau}(H_{n+1}^{\pm2}R_{n+1}^\pm(\tau) + G_{n+1}^{\pm2}R_{n+1}^\mp(\tau))d\tau. \tag{8}$$

Here, the condition of the upper limit of the number of photons initially in the system is considered [36].

To investigate the optical tomography dynamics of the generated dissipative coherent cavity field due to atom-cavity interactions, we focus on the case where the atom starts with the excited state, i.e., $\hat{\rho}_A(0) = |1\rangle\langle 1|$. While the cavity is initially filled by a coherent field or an even coherent field, i.e., $\hat{\rho}_F(0) = |\varphi\rangle\langle\varphi|$,

$$|\varphi\rangle = \sum_{n=0}^{\infty}P_n|n\rangle = \sum_{n=0}^{\infty}\frac{[\frac{\alpha^n}{\sqrt{n!}} + r\frac{(-\alpha)^n}{\sqrt{n!}}]}{\sqrt{[1+r^2+2r\exp(-2|\alpha|^2)]}}e^{-\frac{|\alpha|^2}{2}}|n\rangle, \tag{9}$$

The $|\varphi\rangle$-state is reduced to the coherent state if $r = 0$, and the even coherent state when $r = 1$. By using Eqs. (6), (8), (9), the density matrix $\rho(t)$ of the time-dependent atom-cavity state expression can be expressed as

$$\hat{\rho}(t) = \sum_{m,n=0}[\rho_{m,n}^{11}|\varpi_1\rangle\langle\varpi_1| + \rho_{m,n}^{10}|\varpi_1\rangle\langle\varpi_2| + \rho_{m,n}^{01}|\varpi_2\rangle\langle\varpi_1| + \rho_{m,n}^{00}|\varpi_2\rangle\langle\varpi_2|], \tag{10}$$

where, with $\tilde{R}_{mn}^{\pm\mp}(t) = e^{-i(E_m^\pm - E_n^\mp)t}R_{mn}^{\pm\mp}(t)$, the elements $\rho_{m,n}^{jk}(jk = 0,1)$ are given by:

$$\rho_{m,n}^{11} = \begin{cases}\sum_{jk}X_m^jX_n^k\tilde{R}_{mn}^{jk}(t), & m \neq n;\\[2ex] X_n^{+2}R_n^+(t) + X_n^{-2}R_n^-(t)\\ \quad +2P_n^*P_nX_n^{2+}X_n^{2+}e^{-\gamma(2n+1)t}\cos(2\eta_nt), & m = n.\end{cases}$$

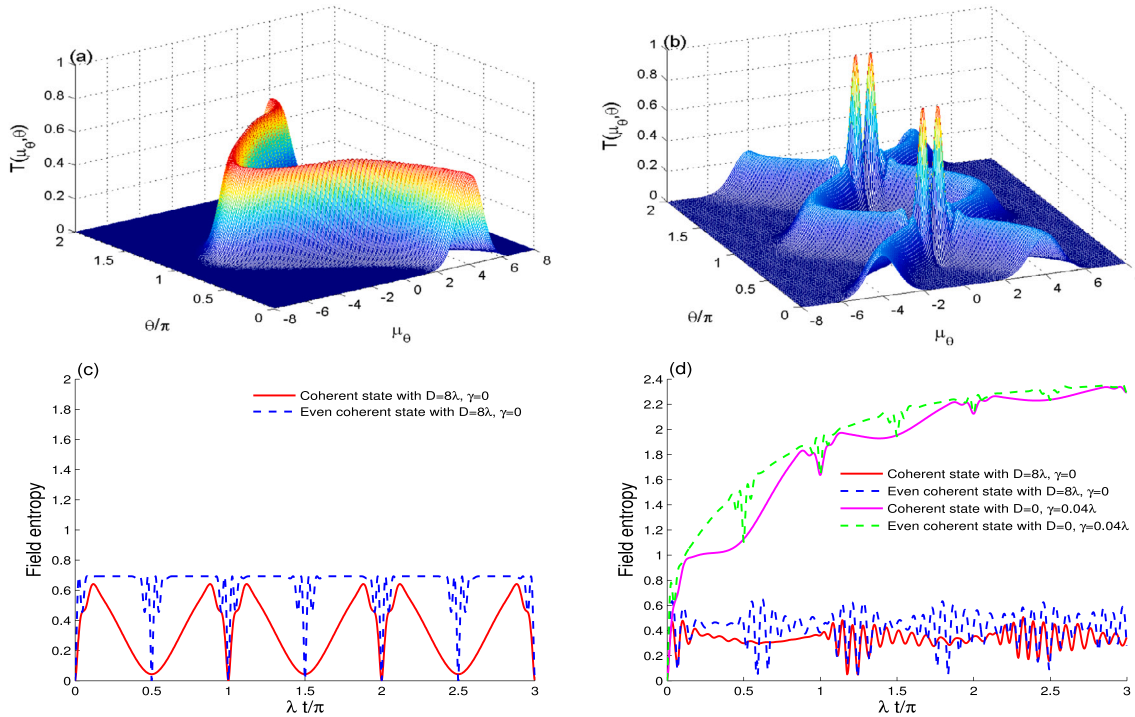

Fig. 1. The optical tomography distributions of the cavity states at the times $\lambda t = n\pi (n = 0, 1, 2, \ldots)$ for the initial coherent state in (a), the even-coherent state in (b). They are plotted with $\alpha = 3$. In (c) and (d), the cavity entropy dynamics is depicted under the effects of cavity damping and the detuning.

$$\rho^{00}_{m,n} = \begin{cases} X_m^- \Phi_n^- \tilde{R}^{++}_{mn}(t) + X_m^+ X_n^+ \tilde{R}^{--}_{mn}(t) - X_m^- X_n^+ \tilde{R}^{+-}_{mn}(t) \\ \qquad - X_m^+ X_n^- \tilde{R}^{-+}_{mn}(t), & m \neq n; \\ X_n^{-2} R_n^+(t) + X_n^{+2} R_n^-(t) \\ \qquad -2P_n^* P_n X_n^{+2} X_n^{+2} e^{-\gamma(2n+1)t}\cos(2\eta_n t), & m = n. \end{cases}$$

$$\rho^{10}_{m,n} = (\rho^{01}_{m,n})^\dagger = X_m^- X_n^+ \tilde{R}^{++}_{mn}(t) X_m^+ X_n^- \tilde{R}^{--}_{mn}(t) + X_m^- X_n^- \tilde{R}^{+-}_{mn}(t) X_m^+ X_n^+ \tilde{R}^{-+}_{mn}(t).$$

To study the optical tomography distributions for the generated coherent cavity-field states, we need only the time-dependent coherent cavity-field states, which are determined by tracing the atom states from the system density matrix $\hat{\rho}(t)$ of Eq. (10),

$$\hat{\rho}_F(t) = \sum_{m,n=0} [\rho^{11}_{m,n} |n\rangle\langle n| + \rho^{00}_{m,n} |n+1\rangle\langle n+1|]. \tag{11}$$

Optical tomography

For $\hat{\rho}_F(t)$ of Eq. (11), the optical coherent-field tomography is given by [4]

$$T(\mu_\theta, \theta, t) = \sum_{m,n=0} [\rho^{11}_{m,n} \langle \hat{\mu}_\theta | n\rangle\langle n|\hat{\mu}_\theta\rangle + \rho^{00}_{m,n} \langle \hat{\mu}_\theta | n+1\rangle\langle n+1|\hat{\mu}_\theta\rangle], \tag{12}$$

where θ is the local oscillator phase, while μ_θ and $|\hat{\mu}_\theta\rangle$ are the eigenvalue and the eigenstate of the operator

$$\hat{\mu}_\theta = \frac{1}{\sqrt{2}}(\hat{\psi} e^{-i\theta} + \hat{\psi}^\dagger e^{i\theta}), \tag{13}$$

Eq. (12) verifies the normalization relation

$$\int T(\mu_\theta, \theta) d\mu_\theta = 1. \tag{14}$$

For the time-dependent coherent cavity-field states $\hat{\rho}_F(t)$ of Eq. (11), the expression of the optical tomography is given by

$$T(\mu_\theta, \theta, t) = \sum_{m,n=0}^{\infty} [\rho^{11}_{mn}(t) K_m(\mu_\theta, \theta) K_n^*(\mu_\theta, \theta) + \rho^{00}_{mn}(t) K_{m+1}(\mu_\theta, \theta) K^*_{n+1}(\mu_\theta, \theta)], \tag{15}$$

with

$$K_m(\mu_\theta, \theta) = \langle \mu_\theta, \theta | m\rangle = \frac{e^{-\frac{\mu_\theta^2}{2}}}{\pi^{\frac{1}{4}}} \frac{e^{-im\theta} H_m(\mu_\theta)}{\sqrt{m! 2^m}}.$$

$H_n(.)$ represents the Hermite polynomial.

Optical tomography dynamics

Here, we explore the generated nonclassical properties's optical tomography's homodyne detector (due to intensity-dependent atom-field interactions) depending on the generated von-Neumann entropy coherence's cavity field at different times, at which the photon-field states have partial and maximal mixedness.

Fig. 1a and b illustrate the optical tomography $T(\Lambda_\theta, \theta, \lambda t = n\pi)$ of the time-dependent coherent cavity-field states at $\lambda t = n\pi (n = 0, 1, 2, \ldots)$ when the cavity is initially filled by the coherent-field state (CFS) in (a), the even coherent-field state (ECFS) of the two "opposite" coherent states $|\pm\alpha\rangle$ in (b), they are plotted for $\alpha = 3$. While Fig. 1(c) and (d) show the field entropy dynamics under the effects of cavity damping and the detuning. The field entropy dynamics is plotted to analyze the cavity field evolution. From Fig. 1(c), we find that the cavity retrieve its initial state at the times $\lambda t = n\pi (n = 0, 1, 2, \ldots)$. For the coherent/even coherent initial field state, the state of the cavity is oscillating from a pure state to a maximally entangled state with $2\pi-$period. Fig. 1(d) shows the cavity damping and the detuning effects. The strong detuning ($D = 8\lambda$) increases the oscillation frequencies and reduces the amplitudes of the cavity entropy. The entropy of the dissipative coherent field cavity with $\gamma = 8\lambda$ grows, i.e. the mixedness of the cavity state enhances while its purity is lost, completely, as they evolves.

Due to that the cavity we retrieve the same initial coherent field or the even coherent field at the time $\lambda t = n\pi (n = 0, 1, 2, \ldots)$ (see Fig. 1(c) and (d)) (see [4–6]). With respect to the μ_θ-axis, Fig. 1(a) shows that the optical CFS (coherent-field state) tomography distribution $T(\mu_\theta, \theta = 0, \lambda t = n\pi)$ appears as symmetric peak around its maximum intensity $\mu_\theta = |\alpha|\sqrt{2}$. While with respect to the θ-axis, the

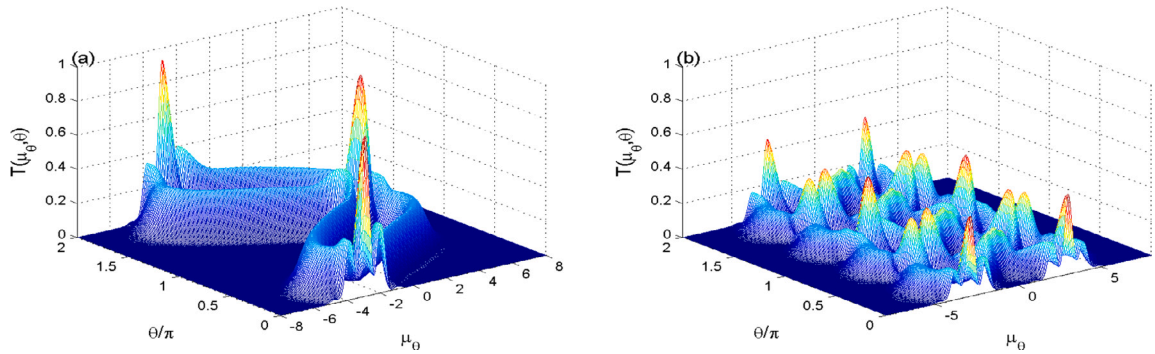

Fig. 2. The dynamics of the optical tomography is plotted at $\lambda t = \frac{3}{4}\pi$ with $\alpha = 3$, $D = 0$, $\gamma = 0$, and for the initial coherent state in (a) and for the initial even coherent state in (b).

optical CFS tomography distribution $|\alpha\rangle$ has a symmetric bottom at $\theta = \pi$. The optical CFS tomography distribution's maximum intensity is independent of μ_θ and θ, and its μ_θ-path performs an oscillatory path that goes through the points $(\mu_\theta, \theta) = (3\sqrt{2}, 0)$, $(\mu_\theta, \theta) = (-3\sqrt{2}, \pi)$, and then the point $(\mu_\theta, \theta) = (3\sqrt{2}, 2\pi)$.

With respect to the μ_θ-axis, Fig. 1(b) illustrates that the optical ECFS (even coherent-field state) tomography distribution has two symmetric peaks around their maximum intensities $\mu_\theta = \pm|\alpha|\sqrt{2}$. In other words, the optical tomography distribution of the superposition of the coherent states $|\alpha\rangle$ and $|-\alpha\rangle$ displays two symmetric distributions in which one of them corresponds to $|\alpha\rangle$ and the other corresponds to $|-\alpha\rangle$. The quantum interference regions between the coherent-field states is reflected in the shape of the tomography distributions for ECFS (even coherent-field state). As θ increases, the optical ECFS tomography distribution moves along two opposite regular π-periodic sinusoidal distributions in the $\mu_\theta - \theta$ plane. The maximum intensity of the optical ECFS tomography distributions is (μ_θ, θ)-independent, except, the intersection regions of the optical ECFS tomography. The maximum intensities rise to two distinct sharp peaks in these intersecting regions.

Fig. 2 illustrates the optical tomography distributions at the times: $\lambda t = \frac{3}{4}\pi$ for the initial coherent state in (a), and for the initial even coherent state in (b). At $\lambda t = \frac{3}{4}\pi$ (see Fig. 2a), the optical CFS-tomography $T(\mu_\theta, \theta, \lambda t = \frac{3}{4}\pi)$ presents different distribution (with respect to the μ_θ-direction) compared to the optical tomography $T(\mu_\theta, \theta, \lambda t = n\pi)$ of Fig. 1a. Except at three places: $(\mu_\theta, \theta) = (-2.95, 0)$, $(\mu_\theta, \theta) = (2.95, \pi)$, and $(\mu_\theta, \theta) = (-2.95, 2\pi)$ the optical CFS tomography is separated into two identical parts of distribution. At each one of these mentioned points, the generated optical CFS-tomography has a peak with a large maximum value. Fig. 2b shows that the atom-ECF interactions have a high ability to generate new different cavity-field states, each one of them characterizes by a unique optical tomography distribution. The optical tomography distribution of the initial coherent state at $\lambda t = \frac{3}{4}\pi$ has regular sinusoidal paths with a $\pi - \theta$-period, which are similar to optical ECFS-tomography sinusoidal paths. Fig. 2b conveys that the generated optical tomography splits into two distributions in two different paths as θ evolves, each of their peak amplitudes is less than that of Fig. 1a.

In Fig. 3, the atom-cavity detuning effect ($D = 8\lambda$) is analyzed for the optical tomography distributions $T(\mu_\theta, \theta, \lambda t = n\pi)(n = 0, 1, 2, \ldots)$ with the same parameters of Fig. 1a,b at the times $\lambda t = n\pi$ with the initial coherent state in (a) and with the initial even coherent state in (b). While, for the resonance case of $D = 8\lambda$, the optical tomography distributions for the initial CFS and for the initial ECFS are illustrated in (c) and (d) at the time $\lambda t = \frac{3}{4}\pi$. We observe that the maximum values, symmetry, and regularity of the CFS/ECFS optical tomography are affected by the detuning. This confirms that atom-ECF interactions can yield new partially/completely cavity-field mixed states. Each of them has a unique form of nonclassicality in terms of optical tomography distribution.

In Fig. 4, the effect of the cavity damping on the optical CFS and ECFS tomography distributions at $\lambda t = \frac{3}{4}\pi$ of Fig. 2 is illustrated for $\gamma = 0.04\lambda$. The cavity damping effect performs new stationary optical tomography distributions.

Fig. 5 illustrates the dynamics of the optical CFS tomography with respect to the space (μ_θ, θ) corresponded to its value's distribution maximum $T_{\max}(-|\alpha|\sqrt{2}, \pi, t)$ in (a) and the optical ECFS tomography maximum $T_{\max}(0.35, 0.5093\pi, t)$ in (b) under the cavity damping and the detuning effects. Because that the optical CFS and ECFS tomographies have periodical dynamics, the discussion can be limited to the time interval $\lambda t \in [0, 5\pi]$. Solid curve of Fig. 5a shows that the CFS tomography $T_{\max}(-|\alpha|\sqrt{2}, \pi, t)$ initiates with a higher values, sequently decreasing and collapsing within a specific time windows. It collapses for a particular time window. The optical CFS tomography then grows to its original maximum value, while performing regular oscillatory dynamics with 2π-period. The non-resonance dash curve shows that the regularity of collapse intervals and the oscillatory dynamics have disappeared. Except for the initial maximum value and collapse interval, the optical CFS tomography maximum values and collapse intervals are lowered. The dash–dot curve of optical CFS tomography shows the influence of cavity damping. The optical CFS tomography maxima values, with the exception of the initial maximum, decrease over time. The maximum optical CFS tomography $T_{\max}(-|\alpha|\sqrt{2}, \pi, t)$ reduces to its non-zero stable optical CFS tomography. Dot curve of the optical CFS tomography indicates that the cavity damping effect can be enhanced by increasing the detuning.

Fig. 5b is plotted for the optical ECFS tomography $T_{\max}(0.35, 0.5093\pi, t)$ under the effects of the cavity dissipation and the detuning. The solid curve illustrates that the optical ECFS tomography oscillatory dynamics have a large maximum $T_{\max}(0.35, 0.5093\pi, t) \approx 1$ and small frequencies. Strong detuning $D = 8\lambda$ leads slightly to decrease the frequencies and increase the amplitudes of irregular oscillatory optical ECFS tomography dynamics. Dash–dot and dot curves illustrate the cavity damping effect for the resonance and non-resonance cases on the oscillatory optical ECFS tomography dynamics. We can deduce that the amplitudes, frequency, regularity, and stability of the oscillatory optical ECFS tomography dynamics depend on the atom-field detuning and the cavity-field damping.

Conclusions

This paper analytically describes the interaction of a two-level atom with a dissipative cavity, characterized by intensity-dependent coupling. The major focus is on examining the optical ECFS tomography distributions while taking detuning and cavity damping into account. Our results show that in the presence of cavity damping, interactions between the atom and the coherent cavity have a remarkable ability to generate novel coherent field states with distinct regularity, amplitude, frequency, and symmetry for both initial coherent and even

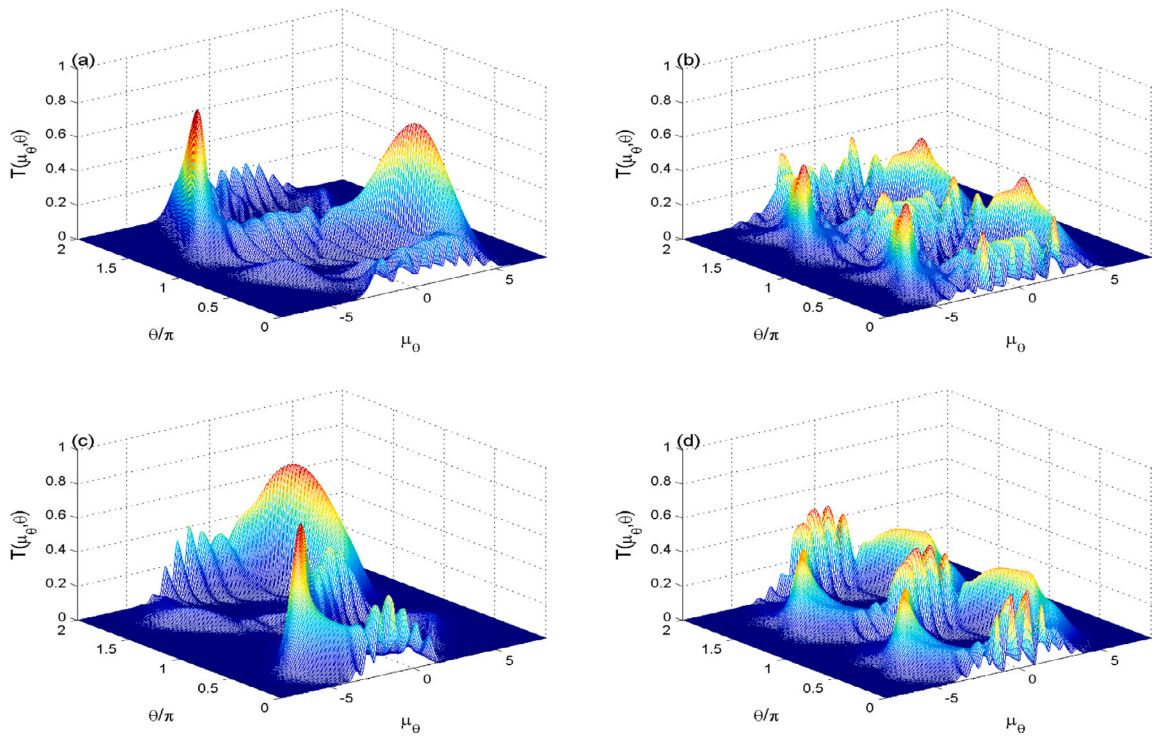

Fig. 3. The effect of the atom-cavity detuning is illustrated on the optical tomography dynamics with $\alpha = 3$, $\gamma = 0$, and $D = 8\lambda$ at the times $\lambda t = n\pi (n = 0, 1, 2, \ldots)$ for the coherent state in (a) and for the even coherent state in (b). While at $\lambda t = \frac{3}{4}\pi$ is for the coherent state in (c) and for the even coherent state in (d).

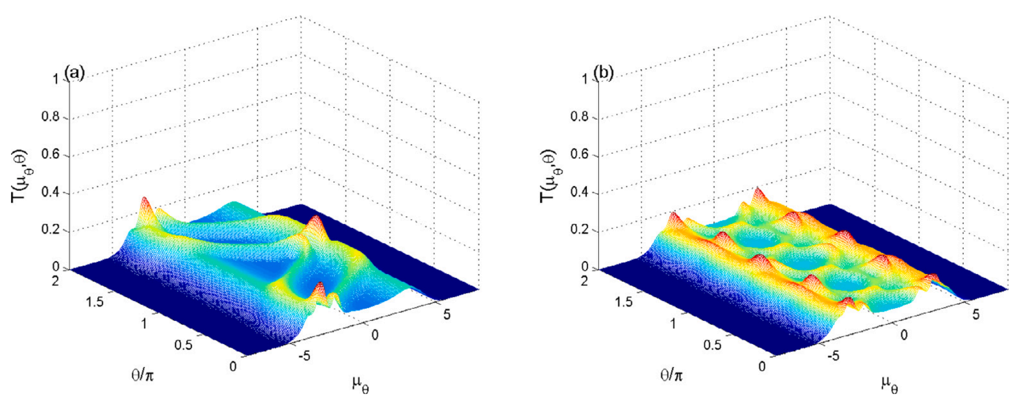

Fig. 4. The effect of the cavity damping is illustrated on the optical tomography dynamics with $\alpha = 3$, $\gamma = 0.04\lambda$, and $D = 0$ at $\lambda t = \frac{3}{4}\pi$ for the coherent state in (a) and for the even coherent state in (b).

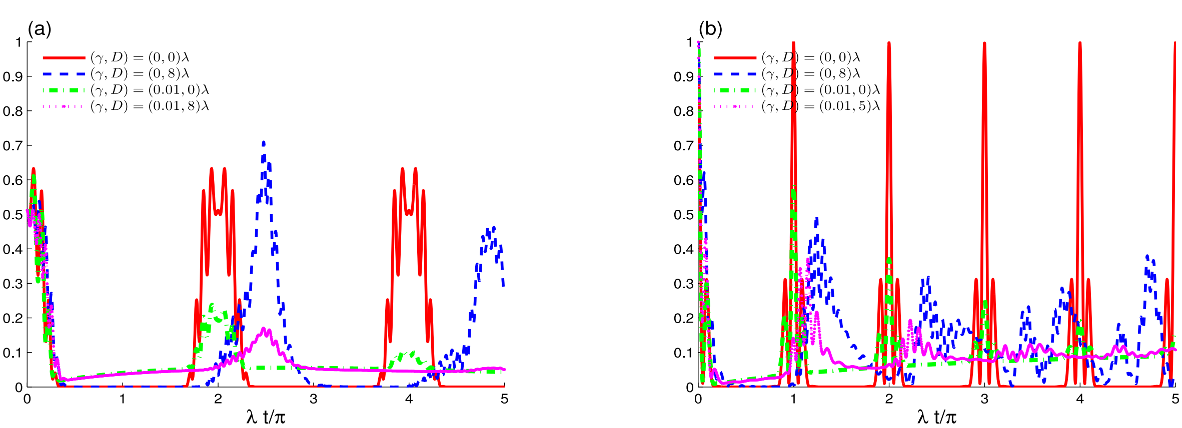

Fig. 5. The maximum-values dynamics of the optical CFS tomography $T_{\max}(-|\alpha|\sqrt{2}, \pi, t)$ in (a) and the optical ECFS tomography $T_{\max}(0.35, 0.5093\pi, t)$ in (b) under the cavity damping and the detuning effects with $|\alpha|^2 = 9$.

coherent states. Notably, when atom-cavity detuning increases, these features become more prominent. Furthermore, the optical tomography distributions produced by these states are particularly sensitive to both cavity field damping and atom-cavity detuning. Our results further reveal that by modifying the atom-field detuning and the cavity damping, the maximum values, frequency, regularity, and stationary value of optical CFS/ECFS tomography can be controlled. In the absence of dissipation, the distribution maxima of both optical CFS and ECFS tomographies exhibit a periodic oscillating pattern for the resonance case. In the absence of dissipation, off-resonance optical tomographies reveal strong oscillations with small amplitudes. Nonetheless, by increasing the dissipation coupling, these oscillations and amplitudes are reduced.

CRediT authorship contribution statement

A.-B.A. Mohamed: Writing – review & editing, Writing – original draft, Software, Methodology, Formal analysis, Conceptualization. **T.A. Alrebdi:** Writing – review & editing, Writing – original draft, Software, Investigation, Conceptualization. **F. Alkallas:** Writing – review & editing, Writing – original draft, Methodology, Formal analysis. **A.-H. Abdel-Aty:** Writing – review & editing, Writing – original draft, Software, Methodology, Conceptualization. **H. Eleuch:** Writing – review & editing, Writing – original draft, Software, Methodology, Conceptualization.

Declaration of competing interest

I declare that I have no significant competing financial, professional, or personal interests that might have influenced the performance or presentation of the work. Also, we do not have any conflict with the authors.

Data availability

No data was used for the research described in the article.

Acknowledgments

This research project was funded by the Deanship of Scientific Research, Princess Nourah bint Abdulrahman University, Saudi Arabia, through the Program of Research Project Funding After Publication, grant No (44-PRFA-P-87). The authors are thankful to the Deanship of Graduate Studies and Scientific Research at University of Bisha for supporting this work through the Fast-Track Research Support Program.

References

[1] Hillery M, O'Connell RF, Scully MO, Wigner EP. Phys Rep 1984;106:121–67.
[2] Vogel K, Risken H. Phys Rev A 1989;40:2847.
[3] Smithey DT, Beck M, Raymer MG, Faridani A. Phys Rev Lett 1993;70:1244–7.
[4] Korennoy YA, Man'ko VI. Phys Rev A 2011;83:053817.
[5] Filippov SN, Man'ko VI. Phys Scr 2011;83:058101.
[6] Miranowicz A, Paprzycka M, Pathak A, Nori F. Phys Rev A 2014;89:033812.
[7] Grandi Samuele, Zavatta Alessandro, Bellini Marco, Paris MatteoGA. New J Phys 2017;19:053015.
[8] Esposito M, Benatti F, Floreanini R, Olivares S, Randi F, Titimbo K, Pividori M, Novelli F, Cilento F, Parmigiani F, Fausti D. New J Phys 2014;16:043004.
[9] Leonhardt U. Measuring the quantum state of light. Cambridge: Cambridge University Press; 1997.
[10] Kravtsov KS, Zhutov AK, Kulik SP. Phys Rev A 2020;102:023706.
[11] Mohamed A-BA, Eleuch H. Sci Rep 2020;10:13240.
[12] Mohamed A-BA, Eleuch H, Raymond Ooi CH. Sci Rep 2019;9:19632, and in; Phys Lett A 2019;383:125905.
[13] Hessian HA, Mohamed A-BA. Laser Phys 2008;18:1217.
[14] Rohith M, Sudheesh C. Phys Rev A 2015;92:053828.
[15] Almarashia AM, Algarnia A, Alabouda FM, Abdel-Khalekb S, Berrada K. Results Phys 2019;14:102352.
[16] Neugebauer M, Fischer L, Jäger A, Czischek S, Jochim S, Weidemüller M, Gärttner M. Phys Rev A 2020;102:042604.
[17] Mohamed A-BA, Khalil EM, Selim MM, Eleuch H. Results Phys 2021;22:103940.
[18] E.T. Jaynes, W. Cummings F. Proc IEEE 1963;51:89.
[19] Tavis M, Cummings FW. Phys Rev 1968;170:379.
[20] Agarwal GS, Puri RR. Phys Rev A 1989;39:2969.
[21] Puri R. Mathematical methods of quantum optics. Heidelberg: Springer Berlin; 2001, http://dx.doi.org/10.1007/978-3-540-44953-9.
[22] Vogel W, de Matos Filho RL. Phys Rev A 1995;52:4214.
[23] Leibfried D, Blatt R, Monroe C, Wineland D. Rev Modern Phys 2003;75:281.
[24] Puebla R, Hwang M-J, Casanova J, Plenio MB. Phys Rev A 2017;95:063844.
[25] Blais A, Huang R-S, Wallraff A, Girvin S, Schoelkopf R. Phys Rev A 2004;69:062320.
[26] Felicetti S, Rossatto DZ, Rico E, Solano E, Forn-Díaz P. Phys Rev A 2018;97:013851.
[27] Huang R, Miranowicz A, Liao J-Q, Nori F, Jing H. Phys Rev Lett 2018;121:153601.
[28] El Anouz K, Onyenegecha CP, Opara AI, Salah Ahmed, El Allati A. J Opt Soc Am B 2022;39:979–89.
[29] Esmail S, Salah Ahmed, Samia SA Hassan. Braz J Phys 2019;49:438–48.
[30] Abdel-Wahab NH, Salah Ahmed. Modern Phys Lett A 2019;34:1950081.
[31] Zare F, Tavassoly MK. Optik 2020;217:164841.
[32] Ghasemian E, Tavassoly MK. Sci Rep 2021;11:3554.
[33] Ghasemian E, Tavassoly MK. Internat J Theoret Phys 2020;59:1742–54.
[34] Ghasemian E, Tavassoly MK. Eur Phys J D 2021;75:103.
[35] Barnett SM, Knight PL. Phys Rev A 1986;33:2444.
[36] Puri RR, Agarwal GS. Phys Rev A 1988;39:3879.
[37] Moya-Cessaa H. Phys Rep 2006;432:1.
[38] Watanabe A, Nakazato H. Ann Physics 2022;441:168890.
[39] Eleuch H, Ben Nessib N, Bennaceur R. Eur Phys J D 2004;29:391.
[40] Abdel-Shafy F Obada, Mohamed MA Ahmed, Ahmed M Farouk, Salah Ahmed. Eur Phys J D 2017;71:338.
[41] Salah Ahmed, Thabet LE, El-Shahat TM, Abd El-Wahab NH, Manal G Edin. Modern Phys Lett A 2022;37:2250030.
[42] Mohamed A-BA, Eleuch H. Sci Rep 2022;12:17162.
[43] Buck B, Sukumar CV. Phys Lett A 1981;81:132.
[44] Valverde C, Goncalves VG, Baseia B. Phys A 2016;446:171.
[45] Berrada K, Al-Rajhi MA. Quantum Inf Process 2017;16:239.
[46] You JQ, Nori F. Physica E 2003;18:33, and in; Phys Rev B 2003;68:064509.